The evolution and arrest of a turbulent stratified oceanic bottom boundary layer over a slope: Upslope regime and PV dynamics

XIAOZHOU RUAN*

Department of Earth, Atmospheric and Planetary Sciences, Massachusetts Institute of Technology, Cambridge, Massachusetts

ANDREW F. THOMPSON

Environmental Science and Engineering, California Institute of Technology, Pasadena, California

JOHN R. TAYLOR

Department of Applied Mathematics and Theoretical Physics, University of Cambridge, Cambridge, UK

**Corresponding author address:* Xiaozhou Ruan, Department of Earth, Atmospheric and Planetary Sciences, Massachusetts Institute of Technology, 77 Massachusetts Ave, Cambridge, MA 02139.

E-mail: xruan@mit.edu

ABSTRACT

The influence of a sloping bottom and stratification on the evolution of an oceanic bottom boundary layer (BBL) in the presence of a mean flow is explored. As a complement to an earlier study (Ruan et al. 2019) examining Ekman arrest in a downslope regime, this paper describes turbulence and BBL dynamics during Ekman arrest in the upslope regime. In the upslope regime, an enhanced stratification develops in response to the upslope Ekman transport and suppresses turbulence. Using a suite of large-eddy simulations, we show that the BBL evolution can be described in a self-similar framework based on a non-dimensional number X/X_a. This non-dimensional number is defined as the ratio between the lateral displacement of density surfaces across the slope X and a displacement X_a required for Ekman arrest; the latter can be predicted from external parameters. Additionally, the evolution of the depth-integrated potential vorticity is considered in both upslope and downslope regimes. The PV destruction rate in the downslope regime is found to be twice the production rate in the upslope regime, using the same definition for the bottom mixed layer thickness. It is shown that this asymmetry is associated with the depth scale over which turbulent stresses are active. These results are a step towards improving parameterizations of BBL properties and evolution over sloping topography in coarse-resolution ocean models.

1. Introduction

In the oceanic bottom boundary layer (BBL), small-scale turbulence extracts energy and momentum from larger scale currents. While the energy input rate by wind stress is relatively well quantified from satellite observations (e.g. Wunsch 1998; Scott and Xu 2009), the closure of the kinetic energy (KE) budget for balanced flows in the ocean, which includes mesoscale eddies and gyres as well as overturning circulations, has been elusive due to large uncertainties associated with key energy sinks. One of the primary energy sinks is bottom drag acting on geostrophic flows (Wunsch and Ferrari 2004). Although a number of recent studies have focused on a global quantification of bottom drag (Wunsch and Ferrari 2004; Sen et al. 2008; Arbic et al. 2009; Wright et al. 2013), large discrepancies remain among the various estimates.

One process that can introduce significant errors in the bottom drag calculation is Ekman arrest (MacCready and Rhines 1991). When a balanced, along-slope mean flow is present over sloping topography, a bottom Ekman layer forms due to the balance between the Coriolis force and bottom friction in the momentum budget. Depending on the direction of the mean flow, the associated cross-slope Ekman transport advects density surfaces, or isopycnals, either upslope or downslope. This advection, along with any turbulent mixing that may occur, produces lateral density gradients and a geostrophic velocity shear that always opposes the mean flow, thus reducing the magnitude of the total along-slope velocity near the bottom (see Fig. 1a for the upslope case). An equilibrium can be reached in which the buoyancy force in the cross-slope direction becomes large enough to balance the Coriolis force. In this limit there is negligible bottom stress and Ekman transport – the arrested state.

The general evolution of the Ekman arrest process, especially the time required for Ekman arrest to reach equilibrium has been studied with various turbulence closures (Weatherly and Martin

1978; Trowbridge and Lentz 1991; MacCready and Rhines 1991; Brink and Lentz 2010; Umlauf et al. 2015). However, resolving the turbulence in the BBL is desirable in order to understand how intermittent and abrupt transitions in turbulent intensities respond to the stratification and shear stress that vary significantly during the approach to Ekman arrest. Both stratification and shear stress influence the maintenance and production of turbulence, and their impacts on turbulence are challenging to reproduce with simple turbulence parameterizations. Thus, one goal of this study is to examine Ekman arrest dynamics in simulations where most of the BBL turbulence is resolved in the Large-Eddy Simulations (LES).

The temporal evolution of the BBL as it approaches Ekman arrest has been explored in previous studies in which the focus has been on how key parameters, such as the background stratification and slope angle, influence adjustment timescales. However, in practice, it is difficult to apply these studies to observations in order to estimate the magnitude of the bottom stress, Ekman transport or other friction-related quantities because of the instantaneous nature of most oceanic measurements. Ruan et al. (2019) addressed this limitation and proposed a new framework that classifies and identifies various BBL stages during Ekman arrest based on measurable environmental variables. This framework was explored for the downslope regime, and spanned stages from fully-turbulent flat-bottom cases to Ekman arrested states. This framework is centered around two length scales. First, the Ekman arrest height H_a describes the bottom mixed layer (BML) thickness needed to achieve Ekman arrest for given values of the stratification, mean flow strength, and slope angle. Second, the relaminarization height H_L describes the BBL thickness at the time when the BBL relaminarizes. The ratio of the evolving BML thickness H and H_a can be used to describe the Ekman arrest process based on instantaneous measurements of the environmental variables, while the ratio between H and H_L can be used to predict when the BBL relaminarizes. In this paper, we extend the framework in Ruan et al. (2019) to the upslope regime.

Momentum and buoyancy budgets are coupled during Ekman arrest, such that Ekman flow transports buoyancy up-/downslope, which in turn affects the flow field. It is challenging, however, to parameterize individual components, such as the stratification and velocity shear, during Ekman arrest in coarse-resolution numerical models that do not resolve the BBL. Progress can be made by combining both the momentum and buoyancy equations in a conserved quantity, the Ertel potential vorticity (PV). Moreover, the PV can be used to identify and predict the onset of submesoscale instabilities (Thomas et al. 2013), which can lead to enhanced energy dissipation and efficient tracer (heat, salt and nutrient) exchange between the boundary layer and interior (Wenegrat and Thomas 2020). With a goal toward a better representation of BBL evolution in numerical models, we provide a parameterization for the evolution of the integrated PV across the BBL for both up- and downslope regimes during Ekman arrest.

The paper is organized as follows: we first introduce our theoretical predictions for the upslope case in section 2; validation of the theoretical predictions and results from the turbulence-resolving simulations are provided in section 3; the evolution of PV and the parameterization of the depth-integrated PV in the BBL in both up- and downslope regimes are described in section 4; the conclusions are summarized in section 5.

2. Theoretical predictions

Similar to the Ekman arrest height H_a, introduced by Ruan et al. (2019) for the downslope regime and diagnosed from external enviornmental parameters, we derive an expression for a length scale associated with arrest in the upslope case. As described below, we use a horizontal, rather than a vertical, length scale in the upslope regime. There are two stages of adjustment when an upwelling favorable mean flow is initialized from rest over a sloping bottom (Fig. 1b) (Brink and Lentz 2010): i) a BML forms with an initial thickness H; ii) isopycnals are advected upslope, which re-stratifies the BBL and suppresses turbulence until the arrested state is achieved. Throughout the manuscript, we define the thickness of the BML using a stratification threshold, referenced to the background stratification N_∞^2. The BML is defined as the depth where N^2 first equals rN_∞^2, where $r = 0.3$. The BML thickness is not sensitive to the value of r; a range of $0.2 < r < 0.4$ yields approximately the same diagnostics (figure not shown). In the downslope regime, the BML is always well-mixed. In contrast, a weak but non-negligible stratification ($N^2 \approx 0.1N_\infty^2$) remains within the BML in the upslope regime. Despite this difference in stratification, across both regimes the BML consistently characterizes the near-bottom layer where isopycnal tilting is strong in response to external mean flows.

Our focus in this study is on stage (ii), the advection of isopycnals, as this likely represents the bulk of the adjustment in the real ocean. In the downslope regime, the evolving thickness of the BML provided the length scale we used to describe the Ekman arrest adjustment — displacement of isopycnals across the slope can be converted to a height scale through the slope angle ($H = \alpha X$) when isopycnals tilt downward. In the upslope regime the BML thickness does not change proportionally with the isopycnal displacement. Instead, a greater upslope displacement will lead to a stronger stratification and a thinner BML. Therefore, we instead use X, the displacement of isopycnals in the cross-slope direction, to describe the Ekman arrest adjustment in the upslope regime.

To leading order, the cross-slope momentum equation in the rotated coordinates shown in Fig. 1a (Weatherly and Martin 1978) is given by

$$\frac{\partial u}{\partial t} - fv = -\alpha b - \frac{1}{\rho_0}\frac{\partial \tau^x}{\partial z}. \tag{1}$$

Here u and v are the perturbation velocities to the background mean flow, f is the Coriolis frequency, α is the inclination angle of a planar slope, τ^x is the cross-slope turbulent stress, and

$b = -g\rho'/\rho_0$ is buoyancy defined as a perturbation away from the background density profile that has a constant stratification N_∞^2, and ρ_0 is a reference density. The small angle approximation is assumed throughout this study. Expressions for the Coriolis force (per unit mass) F_C and buoyancy force (per unit mass) F_B (e.g. Umlauf et al. 2015) at the bottom that balance at the arrested state are

$$F_C = fV_\infty, \qquad F_B = \alpha b = \alpha^2 N_\infty^2 X, \tag{2}$$

where V_∞ is the magnitude of the barotropic along-slope flow. Equating the two forces in the arrested state yields a prediction for the required displacement of isopycnals across the slope:

$$X_a = \frac{fV_\infty}{\alpha^2 N_\infty^2}. \tag{3}$$

Stronger barotropic flow (V_∞), smaller bottom slope, and weaker background stratification increase the equilibrium isopycnal displacement. For typical abyssal ocean parameters: $f = 10^{-4}$ s^{-1}, $V_\infty = 0.05$ m s^{-1}, $\alpha = 5\times10^{-3}$, and $N_\infty^2 = 10^{-7}$ s^{-2}, such that $X_a = 2\times10^6$ m. In contrast, over a moderate continental slope, parameters can be adjusted to $f = 10^{-4}$ s^{-1}, $V_\infty = 0.1$ ms^{-1}, $\alpha = 10^{-2}$, and $N_\infty^2 = 10^{-6}$ s^{-2}, and X_a is reduced by over an order of magnitude to 10^5 m. In the next section, we show that the ratio between the evolving isopycnal displacement across the slope X and the isopycnal displacement in a state of Ekman arrest, X_a, forms a non-dimensional number that describes the BBL evolution in the upslope regime.

In the boundary layer with a nonzero buoyancy flux at the boundary, the competition between shear production and buoyancy flux in maintaining the turbulence can be characterized by the Obukhov length scale. Here, we assume that the buoyancy flux at the sloping bottom (e.g. due to geothermal heating) is zero. However, as discussed in Ruan et al. (2019), we can define a 'slope Obukhov length' in an analogous way to the Obukhov length by replacing the surface buoyancy flux in the slope-normal direction with the cross-slope Ekman buoyancy flux. This bottom-stress-driven Ekman buoyancy flux has similarities to the wind-driven Ekman buoyancy flux in the surface boundary layer (Thomas 2005). In the BBL, the lateral density gradient arises from a sloping bottom intersecting a vertical stratification, whereas in the surface ocean, the lateral density gradient typically arises from frontal dynamics that allow a range of density surfaces to outcrop in the mixed layer. The slope Obukhov length can thus be defined as (see Ruan et al. (2019) for detailed derivation):

$$L_s = (1+Bu^2)\frac{fu_*}{k\alpha N_\infty^2}, \tag{4}$$

where $Bu = \alpha N_\infty f^{-1}$ is the slope Burger number, $k = 0.41$ is the von Karman constant and $u_* \equiv \sqrt{\tau^y/\rho}$ is the friction velocity. As discussed in Ruan et al. (2019), L_s can be non-dimensionalized by the viscous length scale $\delta_\nu = \nu/u_*$ (ν is the molecular viscosity):

$$L_s^+ = \frac{L_s u_*}{\nu} = (1+Bu^2)\frac{f{u_*}^2}{\nu k\alpha N_\infty^2}, \tag{5}$$

to form the viscous slope Obukhov length, L_s^+. It has been shown that L_s^+ describes the turbulent state in the downslope Ekman arrest regime, such that for $L_s^+ < 100$, turbulence collapses and the boundary layer enters a relaminarized state (Ruan et al. 2019). The connection between L_s^+ and the turbulent state of the BBL also enables us to predict the magnitude of friction-related quantities such as the friction velocity, wall stress and cross-slope Ekman transport, when the turbulence is suppressed and the BBL relaminarizes. Our working hypothesis is that the BBL relaminarizes when L_s^+ falls below some critical value in the upslope regime.

3. Ekman arrest in the upslope regime

A suite of LES are performed with a variety of slope angles, background stratification and barotropic mean flow magnitudes (Table 1 with the suffix “-u” denoting the upslope simulations) using the computational fluid dynamics solver, DIABLO. Details of the numerical method used in DIABLO can be found in Taylor (2008) and Bewley (2008). In order to resolve the turbulence close to the smooth solid bottom, we performed LES with near-wall resolution which resolves at least 80% of the energy throughout the BBL (Pope 2001; Sagaut 2006). In particular, the resolution is sufficiently high to capture viscous effects near the wall and thus minimize the reliance on the Smagorinsky subgrid-scale model. The domain size is 30 m (L_x) in the x and y directions and 60 m (L_z) in the slope-normal (z) direction. In order to avoid the direct impact of stratification on turbulence development near the wall, we constructed a thin (~ 2 m) mixed layer near the bottom in the initial stratification profile. Other details of the simulation setup, including the initial stratification profile, are provided in section 3 of Ruan et al. (2019), thus are not included here to avoid repetition.

As the isopycnals are advected upslope, the buoyancy force, F_B in (2), starts to oppose the flow in the cross-slope direction. The evolution of the total cross- and along-slope flow in simulation A-u and F-u are shown in Fig. 2. Simulation A-u has the smallest slope angle $\alpha = 0.005$ and weakest background stratification $N_\infty^2 = 10^{-7}\mathrm{s}^{-2}$, and thus is close to the flat-bottom Ekman layer limit. Simulation F-u, on the other hand, has a large slope angle $\alpha = 0.02$ and strong stratification $N_\infty^2 = 10^{-5}\mathrm{s}^{-2}$, and evolves rapidly toward the Ekman-arrested state. The cross-slope velocity and depth-integrated transport in simulation F-u decays to around 0 after a non-dimensional time $tf = 20$, whereas simulation A-u exhibits a relatively steady flow field (Figs. 2a, c and 3). Simulation A-u also shows relatively little reduction in the near-bottom along-slope mean flow, especially compared with simulation F-u (Fig. 2b, d). Oscillations are a prominent feature of the cross-slope flows and have near-inertial frequencies that are determined by the slope angle and background stratification (Brink and Lentz 2010) (Figs. 2a, c and 3). Around $tf = 20$, when the cross-slope flow stabilizes, simulation F-u shows a negligible (period-averaged) cross-slope velocity and large velocity cancellation between the boundary layer (perturbation) and far-field flows in the along-slope direction in the BBL (Fig. 4). A major difference between the upslope and downslope regimes is that in the downslope regime, the BML deepens as isopycnals tilt downward and the near-bottom flow is reduced due to the increasingly greater thickness of the boundary layer over which the thermal wind shear is present. In the upslope regime, the flow reduction is realized by enhanced buoyancy gradients in the horizontal direction, and a progressively stronger thermal wind shear is found over a vertical length scale that remains relatively unchanged (Fig. 5).

Two different end states of the boundary layer stratification are found in Brink and Lentz (2010). In cases with large *Bu*, the enhanced stratification near the bottom connects smoothly with the interior stratification at the arrested state, whereas for cases with small *Bu*, a density jump, or a "cap," is present that separates two linearly-stratified regions within and outside of the BBL. The LES simulations do not produce a capped upwelling case in the arrested state, even for experiments with small *Bu* (our simulation H-u). The absence of the density jump could be related to the treatment of turbulence between our LES experiments and models with typical second-order turbulence closures. Moreover, the relaminarization process (discussed below), which destroys the BML at the arrested state, could contribute to this discrepancy, although more simulations with small *Bu* that reach the arrested state are needed to confirm this. Additionally, the constant gradient Richardson number in the arrested BBL, as reported by Brink and Lentz (2010), does not exist in our simulations (figure not shown).

During Ekman arrest, stratification is enhanced in the BBL (Fig. 5) and turbulence is expected to be suppressed (e.g. Taylor and Sarkar 2008; Deusebio et al. 2014). We show the evolution of turbulent kinetic energy (TKE) in two of the runs in which the TKE becomes negligible (Fig. 6). TKE in simulations F-u and H-u has its largest magnitude at the beginning of the simulation before the isopycnals are advected upslope, then TKE decays sharply with time as stratification strengthens close to the bottom until the turbulence is completely suppressed (Figs. 5 and 6a, b).

The decay of TKE is the result of i) a reduced friction velocity (or bottom stress) as the total near-bottom flow weakens (Figs. 2d and 6c, d) and the turbulence production rate slows; ii) a stronger stratification that suppresses turbulence. In both experiments F-u and H-u, the collapse of TKE coincides with the time when L_s^+ falls below 100 (Fig. 6c, d). This relaminarization threshold is consistent with the simulations in the downslope regime, such that turbulence collapse occurs when stable stratification penetrates into the viscous wall region ($\sim 100\nu/u_*$) (Ruan et al. 2019). Thus, a prediction for the friction velocity and other related quantities can be given when the BBL relaminarizes:

$$u_*^2 = \frac{100\nu k \alpha N_\infty^2}{f(1+Bu^2)}. \tag{6}$$

Once the flow becomes laminar, L_s^+ and u_* evolve slowly in time in response to molecular diffusion (Fig. 6c, d).

We note that a limitation of the LES simulations is that they do not account for bottom roughness and this may impact the prediction in (6). However, the use of a non-dimensional Obukhov length threshold to predict turbulence collapse has been confirmed in a range of settings including DNS with a smooth bottom, laboratory experiments with rough bottom, and *in-situ* observations in the atmospheric boundary layers (Flores and Riley 2011). This suggests that the diagnosed threshold for relaminarization during Ekman arrest ($L_s^+ < 100$) can be extended to a rough bottom and higher Reynolds numbers as long as the height of the roughness is not large enough to disrupt the buffer layer where viscous effects give way to the log-law region (Jiménez 2004). However, future studies would be required to confirm this.

Next we examine the evolution of the friction velocity, u_*, a measure of the friction (or bottom stress) exerted by the solid bottom, in all the simulations. For the simulations where Bu is small (*e.g.* A-u, B-u and C-u), there are relatively little changes to the friction velocity throughout the simulations (Fig. 7a). In contrast, when Bu is large (*e.g.* F-u and H-u), the friction velocity decays sharply with time. The much slower evolution of u_* in the later stage of simulations F-u and H-u is related to the relaminarized state described above. Although the timescale required to reach equilibrium varies by orders of magnitude across the different simulations, we anticipate that all simulations will eventually reach the arrested state. However, for small Bu, the time required for the arrest to be achieved is too long to capture in the LES. The relatively small changes in u_* in the simulations with small Bu indicate that they remain far away from arrest at the end of the simulation.

The change in friction velocity can be described in terms of the non-dimensional number X/X_a. Here, we define the ratio between the distance over which isopycnals move across the slope, $X = b/(\alpha N_\infty^2)$, and the required displacement X_a for Ekman arrest defined in (3). When plotted against X/X_a, the friction velocity collapses onto a linear relationship for all simulations (Fig. 7b):

$$u_* = u_{*0}(1 - X/X_a), \tag{7}$$

where u_{*0} is the initial friction velocity with flat isopycnals. Stages far from arrest correspond to regions where $X/X_a \ll 1$ and $u_*/u_{*0} \approx 1$ and those close to the arrested states are characterized by enhanced X/X_a and reduced u_*/u_{*0} (Fig. 7b). Two simulations enter the relaminarized state before X/X_a reaches 1, which indicates that relaminarization occurs before the Ekman arrested state, which is similar to the downslope regime. Data points for simulations F-u and H-u for the times when L_s^+ falls below 100 are not shown because of the slower evolution in the relaminarized states.

The non-dimensional ratio, X/X_a provides a useful way to diagnose the state of the BBL in the upslope regime. Note that X_a depends only on environmental parameters, such as the magnitude of the topographic slope, interior stratification and the strength of the background flow. Thus, given X_a, the friction velocity can be predicted based on the non-dimensional parameter X/X_a, where the lateral displacement of isopycnals X are available from instantaneous observations of the ambient environment[1]. In other words, the full evolution of the upslope isopycnal displacement need not be observed.

4. PV evolution

During Ekman arrest, the momentum and buoyancy budgets are coupled over the sloping bottom, which complicates the analysis of the bulk BBL evolution. Here, we combine both the momentum and buoyancy into a single materially-conserved quantity, the Ertel PV. The Ertel PV is a useful tool for developing parameterizations in numerical models as it overcomes the need to describe each individual component in the momentum and buoyancy budgets of the BBL evolution. The PV also provides a convenient measure for the condition when the flow becomes unstable to various types of hydrodynamic, typically submesoscale, instabilities (Thomas et al. 2013). We discuss the evolution of the point-wise and depth-integrated PV in the BBL for both the upslope and downslope regimes during Ekman arrest (simulation details are summarized in Table 2 with suffix "-d"). The Ertel PV is defined as:

$$q = \omega_a \cdot \nabla B, \tag{8}$$

where $\omega_a = \nabla \times \mathbf{u} + f\hat{\mathbf{z}}$ is the absolute vorticity ($\hat{\mathbf{z}}$ denotes the local vertical direction) and $\nabla B = \nabla b + N_\infty^2 \hat{\mathbf{z}}$ is the total buoyancy gradient. When q takes the opposite sign of the local Coriolis parameter f in a stably stratified environment, symmetric and centrifugal/inertial instabilities can be induced; these instabilities extract energy through either the vertical or lateral geostrophic shear, respectively (Haine and Marshall 1998; Thomas et al. 2013). These submesoscale instabilities

[1]The length scale X is obtained from the ratio of the density difference arising from isopycnal tilting—*i.e.* the difference between the observed seafloor density and the density expected from the incropping of an unperturbed, vertical, interior stratification—and the cross-slope density gradient at the seafloor.

also provide strong constraints on the BBL evolution, as they tend to bring the BBL to marginal stability, a state with zero boundary layer PV (Wenegrat and Thomas 2020).

Changes in PV horizontally-averaged over the doubly-periodic domain are determined by the convergence/divergence of the slope-normal PV flux (Marshall and Nurser 1992; Thomas 2005; Taylor and Ferrari 2010):

$$\frac{\partial < q >}{\partial t} + \frac{\partial < J^z >}{\partial z} = 0, \tag{9}$$

where angle brackets denote a spatial average in the x and y directions and J^z is the slope-normal component of the full PV flux:

$$\mathbf{J} = \mathbf{u}q + \nabla B \times \mathbf{F} - \mathscr{D}\omega_a. \tag{10}$$

Here $\mathbf{F} = \nu\nabla^2\mathbf{u}$ and $\mathscr{D} = \kappa\nabla^2 b$. The three terms in (10) denote the advective, frictional and diabatic components of the PV flux. In the rotated coordinate in the sloping BBL, PV takes the following form (using the small-angle approximation):

$$< q > = f\frac{\partial < b >}{\partial z} + fN_\infty^2 + N_\infty^2\alpha\frac{\partial < v >}{\partial z} + \frac{\partial < b'\zeta' >}{\partial z}, \tag{11}$$

where $\zeta = \frac{\partial v}{\partial x}$ is the relative vorticity in the slope normal direction for a 2D system.

The evolution of $< q >$ is shown in Fig. 8 for two cases, one for the downslope regime and one for the upslope regime, both far from arrest. We ignore the last term in equation (11) as the contribution is small for timescales longer than an inertial period (Taylor and Ferrari 2010); also this correlation term vanishes in the depth-integrated budget that we consider next. For the downslope regime, the total PV decreases from its initial value (Fig. 8c). As isopycnals tilt downwards in the BBL, the thickness of the layer with zero or negative PV increases (Fig. 8a). During the adjustment toward Ekman arrest, the total stratification is weakened, and at the same time the vertical shear of the along-slope flow is enhanced, leading to a decay in both the PV and the depth-integrated PV (Fig. 8a, c). The PV destruction rate undergoes a rapid adjustment as the BML forms and becomes steadier as the simulation approaches arrest. In the upslope regime, the trend is reversed as the total stratification increases and the velocity shear takes the opposite sign to that in the downslope regime. In contrast to the downslope regime, the thickness of the layer corresponding to low PV values changes more slowly after the initial adjustment stage. Furthermore, the PV production rate remains relatively steady throughout the simulation, except for cases with small Bu where the initial thickening of the BML reduces the PV. This reduction in PV later reverses as restratification dominates the PV evolution (figure not shown).

We next analyze the evolution of the depth-integrated PV by integrating equation (9) from the bottom to a depth (beyond the BBL) where the vertical PV fluxes become negligible. Because of the presence of a solid bottom, the advective PV flux vanishes at $z = 0$ due to the no normal flow boundary condition. The diffusive PV flux is small due to both the insulating bottom boundary condition at $z = 0$ and the well-mixed layer with near-zero stratification adjacent to the bottom (Fig. 5b). Thus, the depth-integrated PV is only determined by the frictional flux at the bottom, such that when the PV flux is directed out of the BBL, the integrated PV decreases and vice versa:

$$\frac{\partial}{\partial t}\int_0^\infty q\,\mathrm{d}z = (\nabla B \times \mathbf{F})\big|_{z=0}. \tag{12}$$

The along-slope (y) component of the friction force $\mathbf{F}$ can be rewritten as $F^y = \rho_0^{-1}\partial\tau^{\mathbf{y}}/\partial z$, where τ^y is the viscous shear stress in the along-slope direction. Thus we arrive at the final expression:

$$\frac{\partial}{\partial t}\int_0^\infty q\,\mathrm{d}z = \left(\frac{1}{\rho_0}\frac{\partial B}{\partial x}\frac{\partial \tau^y}{\partial z}\right)\bigg|_{z=0} \sim \frac{\alpha N_\infty^2 u_*^2}{H}. \tag{13}$$

Here the magnitude of the cross-slope buoyancy gradient is αN_∞^2 and we approximate the vertical gradient of shear stress using the bottom stress $\tau_b = \rho_0 u_*^2$ and the thickness of the BML, H, as defined in section 2. We choose to use the thickness of the BML rather than an Ekman layer for the vertical length scale here because these two length scales are often very similar for turbulent Ekman layers (Thomas 2005), at least when they are far from arrest. Also, the mixed layer depth is a convenient and more easily observable metric in practice. Other scaling options were tested for this length scale, including the turbulent Ekman layer, u_*/f, and the viscous sublayer, ν/u_* (as the stress gradient is evaluated at the wall). However, neither of these two resulted in a collapse of the rate of change of the integrated PV, as occurs when using H (figure 9).

We note that the study of Benthuysen and Thomas (2012) found a significant contribution to the PV flux from the diabatic component, but their simulations differ from ours in a couple of key ways. First, because of the initial thin bottom mixed layer at the start of the LES simulations, there is no buoyancy flux across the solid bottom throughout the Ekman adjustment due to the insulating bottom boundary condition. This differs from Benthuysen and Thomas (2012) where isopycnals are initially flat, causing the diabatic PV flux to be large. Furthermore, their frictional PV flux is smaller than ours due to a weaker ($O(1)$cm/s) along-slope flow during the evolution toward Ekman arrest. Our simulations are designed to account for realistic magnitudes of boundary currents that are typically found over the continental slope as well as accounting for a negligible buoyancy flux across the solid bottom.

The ratio between the rate of change of the integrated PV and the frictional PV flux is constant after the initial adjustment in both upslope and downslope regimes (Fig. 9). For the downslope regime (note the negative sign for the downslope regime for PV destruction), the initial deviation away from the constant of proportionality is related to the faster PV reduction rate during the period of convective adjustment as the BML forms. For the upslope regime, all the simulations experience a two-stage adjustment. At the beginning of the simulation, the integrated PV evolution depends sensitively on the formation of BML (increasing H) due to enhanced mixing before restratification takes place. After the BML thickness H equilibrates, the PV production rate stabilizes (Fig. 8d), and a constant proportionality is reached between the two sides of equation (13). Simulations D-u, F-u and H-u in the upslope regime are not included in determining the constant of proportionality because they either entered or are close to the relaminarized state where the PV evolution rate falls off sharply.

For the steady PV evolution following the initial adjustment, the proportionality in the two regimes differs by a factor of two:

$$\frac{\partial}{\partial t}\int_0^\infty q\,\mathrm{d}z \approx -\frac{\alpha N_\infty^2 u_*^2}{H} \quad \text{(downslope)} \tag{14}$$

and

$$\frac{\partial}{\partial t}\int_0^\infty q\,\mathrm{d}z \approx \frac{\alpha N_\infty^2 u_*^2}{2H} \quad \text{(upslope)}. \tag{15}$$

To determine the origin of this difference, we consider the evolution of the vertical turbulent momentum fluxes for two simulations, one in the downslope regime (G-d) and one in the upslope regime (G-u) (Fig. 10). While our definition of the BML thickness captures the height over which turbulent stresses dominate in the downslope regime, it underestimates this height in the upslope regime. For the upslope case, with the enhanced stratification in the BBL, turbulent fluxes are active over a thicker layer than the BML with bursts of turbulent stresses often reaching twice the BML height (Fig. 10). The penetration depth is close to the upper bound of the layer with thermal wind shear and also collocates with the local stratification maximum in the vertical direction. At the same time, the growth of the BML is limited by this enhanced stratification, resulting in a scale separation between the BML and the layer characterized by the thermal wind shear; this scale separation does not exist in the downslope regime. This indicates that with the same definition of the BML thickness based on density, the PV increase rate in the upslope regime is half the destruction rate in the downslope regime.

5. Conclusions and discussions

In this study, we described a suite of turbulence-resolving LES for the Ekman arrest process in the upslope regime and discuss the PV budgets in the upslope and downslope regimes. In the upslope regime, turbulence is increasingly suppressed, following an initial adjustment of the BML, until a laminar state is reached. In both upslope and downslope regimes the slope Obukhov length (L_s^+) predicts when the BBL relaminarizes ($L_s^+ < 100$). From the momentum balance, we also derived a prediction for the cross-slope isopycnal displacement required to achieve Ekman arrest:

$$X_a = \frac{fV_\infty}{\alpha^2 N_\infty^2}.$$

The non-dimensional number X/X_a, which varies between 0 and 1, can be used to identify various stages of Ekman arrest. We note that in the upslope Ekman arrest regime, the BBL reaches the relaminarized state before the Ekman arrested state. This indicates that in the real ocean, the Ekman arrest state in the upslope regime is almost impossible to reach, because background processes (e.g. internal waves and tides) are likely to perturb the relaminarized state before the full Ekman arrested state is reached. This is consistent with the downslope regime, and together can be used to explain the lack of observations of the complete Ekman arrested state in the ocean (e.g. Trowbridge and Lentz 1998). Additionally, we do not observe the "capped" density structure at the arrested state for the upwelling regime (Brink and Lentz 2010); this is due to the relaminarization in our LES simulations which is absent in previous models with simple turbulence closures.

We also examined the evolution of the depth-integrated Ertel PV in both the upslope and downslope regimes where an asymmetry is found in the proportionality between the PV evolution rate and the scaling for the frictional PV flux. Specifically, we arrived at a parameterization for the evolution of the depth-integrated PV, provided in equations (14) and (15). The expression for the downslope regime complements a formula proposed by Wenegrat and Thomas (2020) (their equation 25) that describes the evolution of the PV integrated across the majority of the BBL, but outside of the thin diffusive/viscous layer near the bottom for the downslope Ekman arrest scenario. Thus, the bulk PV evolution in different parts of the BBL can now be quantified in the downslope Ekman arrest regime. From equations (14) and (15), the PV production rate in the upslope regime is half the destruction rate in the downslope regime, given the same definition of BML thickness H. This asymmetry stems from a difference in a characteristic decay scale for the turbulent stress. While in the downslope regime the decay scale is strongly correlated with the BML thickness, the turbulent stresses extend beyond the BML height in the upslope regime. The scale separation between the BML and the layer with thermal wind shear could explain the empirical factor of two difference. We attempted other vertical length scales in (15), but the mixed layer H provided the best collapse of the simulation data.

Due to the small domain size, we do not resolve the BBL submesoscale instabilities that would almost certainly be active in larger domains. While the restratification and enhanced energy dissipation associated with these BBL submesoscale dynamics (e.g. baroclinic, symmetric or centrifugal instabilities) have been identified in previous studies (e.g. Callies 2018; Wenegrat et al. 2018; Ruan and Callies 2020; Wenegrat and Thomas 2020), their parameterizations are still uncertain. For coarse-resolution numerical simulations, the bulk PV parameterizations provided in this study could inform the onset of submesoscale instabilities; an associated state of marginal stability with zero PV is also expected for the BBL with efficient submesoscale adjustments. Thus, the evolution of the integrated PV budget described here will be helpful in future parameterizations of the BBL evolution with external mean flows, especially when combined with parameterizations of the under-resolved submesoscale processes.

Finally, given the proposed H_a in Ruan et al. (2019) and X_a in this study, the Ekman arrest process can be parameterized using the relevant non-dimensional number in the upslope (X/X_a)

and downslope (H/H_a) regimes. This could improve quantitative estimates of the bottom stress given the background stratification, slope angle and mean flow magnitude given observations of X and H, even when the mean flow measurements are far from the BBL. Given the common assumption made in previous global estimates of bottom drag that mean flows observed in the interior are the same as those outside of the BBL, we believe that a revised estimate of the global sink of KE due to bottom drag, accounting for Ekman arrest, will likely decrease. Isopycnals are generally tilted rather than flat leading to a reduction of the total near-bottom flow as compared to the ocean interior. Accurate estimates of this reduction in bottom drag could be obtained with global quantification of H/H_a and X/X_a (depending on the mean flow orientation with respect to the slope) from observations or simulations that do not resolve the velocities close to the bottom. In view of the potentially smaller bottom drag contribution, other KE sinks, including mixing arising from submesoscale processes (Gula et al. 2016; Ruan et al. 2017; Garabato et al. 2019; Wenegrat and Thomas 2020) and lee wave generation/breaking (Nikurashin and Ferrari 2011) associated with flow-topography interactions may play larger roles in the global KE budget.

References

Arbic, B. K., and Coauthors, 2009: Estimates of bottom flows and bottom boundary layer dissipation of the oceanic general circulation from global high-resolution models. *Journal of Geophysical Research: Oceans*, **114 (C2)**.

Benthuysen, J., and L. N. Thomas, 2012: Friction and diapycnal mixing at a slope: Boundary control of potential vorticity. *Journal of physical oceanography*, **42 (9)**, 1509–1523.

Bewley, T. R., 2008: Numerical renaissance: simulation, optimization, and control. *San Diego*.

Brink, K. H., and S. J. Lentz, 2010: Buoyancy arrest and bottom Ekman transport. part I: Steady flow. *Journal of Physical Oceanography*, **40 (4)**, 621–635.

Callies, J., 2018: Restratification of abyssal mixing layers by submesoscale baroclinic eddies. *Journal of Physical Oceanography*, **48 (9)**, 1995–2010.

Deusebio, E., G. Brethouwer, P. Schlatter, and E. Lindborg, 2014: A numerical study of the unstratified and stratified Ekman layer. *Journal of Fluid Mechanics*, **755**, 672–704.

Flores, O., and J. Riley, 2011: Analysis of turbulence collapse in the stably stratified surface layer using direct numerical simulation. *Boundary-Layer Meteorology*, **139 (2)**, 241–259.

Garabato, A. C. N., and Coauthors, 2019: Rapid mixing and exchange of deep-ocean waters in an abyssal boundary current. *Proceedings of the National Academy of Sciences*, **116 (27)**, 13 233–13 238.

Gula, J., M. J. Molemaker, and J. C. McWilliams, 2016: Topographic generation of submesoscale centrifugal instability and energy dissipation. *Nature communications*, **7**, 12 811.

Haine, T. W., and J. Marshall, 1998: Gravitational, symmetric, and baroclinic instability of the ocean mixed layer. *Journal of physical oceanography*, **28 (4)**, 634–658.

Jiménez, J., 2004: Turbulent flows over rough walls. *Annu. Rev. Fluid Mech.*, **36**, 173–196.

MacCready, P., and P. B. Rhines, 1991: Buoyant inhibition of Ekman transport on a slope and its effect on stratified spin-up. *Journal of Fluid Mechanics*, **223**, 631–661.

Marshall, J. C., and A. G. Nurser, 1992: Fluid dynamics of oceanic thermocline ventilation. *Journal of physical oceanography*, **22 (6)**, 583–595.

Nikurashin, M., and R. Ferrari, 2011: Global energy conversion rate from geostrophic flows into internal lee waves in the deep ocean. *Geophysical Research Letters*, **38 (8)**.

Pope, S. B., 2001: Turbulent flows. IOP Publishing.

Ruan, X., and J. Callies, 2020: Mixing-driven mean flows and submesoscale eddies over mid-ocean ridge flanks and fracture zone canyons. *Journal of Physical Oceanography*, **50 (1)**, 175–195.

Ruan, X., A. F. Thompson, M. M. Flexas, and J. Sprintall, 2017: Contribution of topographically generated submesoscale turbulence to Southern Ocean overturning. *Nature Geoscience*, **10 (11)**, 840.

Ruan, X., A. F. Thompson, and J. R. Taylor, 2019: The evolution and arrest of a turbulent stratified oceanic bottom boundary layer over a slope: Downslope regime. *Journal of Physical Oceanography*, **49 (2)**, 469–487.

Sagaut, P., 2006: *Large eddy simulation for incompressible flows: an introduction*. Springer Science & Business Media.

Scott, R. B., and Y. Xu, 2009: An update on the wind power input to the surface geostrophic flow of the world ocean. *Deep Sea Research Part I: Oceanographic Research Papers*, **56 (3)**, 295–304.

Sen, A., R. B. Scott, and B. K. Arbic, 2008: Global energy dissipation rate of deep-ocean low-frequency flows by quadratic bottom boundary layer drag: Computations from current-meter data. *Geophysical Research Letters*, **35 (9)**.

Taylor, J. R., 2008: *Numerical simulations of the stratified oceanic bottom boundary layer*. University of California, San Diego.

Taylor, J. R., and R. Ferrari, 2010: Buoyancy and wind-driven convection at mixed layer density fronts. *Journal of Physical Oceanography*, **40 (6)**, 1222–1242.

Taylor, J. R., and S. Sarkar, 2008: Stratification effects in a bottom Ekman layer. *Journal of Physical oceanography*, **38 (11)**, 2535–2555.

Thomas, L. N., 2005: Destruction of potential vorticity by winds. *Journal of physical oceanography*, **35 (12)**, 2457–2466.

Thomas, L. N., J. R. Taylor, R. Ferrari, and T. M. Joyce, 2013: Symmetric instability in the Gulf Stream. *Deep Sea Research Part II: Topical Studies in Oceanography*, **91**, 96–110.

Trowbridge, J., and S. Lentz, 1991: Asymmetric behavior of an oceanic boundary layer above a sloping bottom. *Journal of Physical Oceanography*, **21 (8)**, 1171–1185.

Trowbridge, J., and S. Lentz, 1998: Dynamics of the bottom boundary layer on the northern California shelf. *Journal of Physical Oceanography*, **28 (10)**, 2075–2093.

Umlauf, L., W. D. Smyth, and J. N. Moum, 2015: Energetics of bottom Ekman layers during buoyancy arrest. *Journal of Physical Oceanography*, **45 (12)**, 3099–3117.

Weatherly, G. L., and P. J. Martin, 1978: On the structure and dynamics of the oceanic bottom boundary layer. *Journal of Physical Oceanography*, **8 (4)**, 557–570.

Wenegrat, J. O., J. Callies, and L. N. Thomas, 2018: Submesoscale baroclinic instability in the bottom boundary layer. *Journal of Physical Oceanography*, **48 (11)**, 2571–2592.

Wenegrat, J. O., and L. N. Thomas, 2020: Centrifugal and symmetric instability during ekman adjustment of the bottom boundary layer. *Journal of Physical Oceanography*, **50 (6)**, 1793–1812.

Wright, C. J., R. B. Scott, D. Furnival, P. Ailliot, and F. Vermet, 2013: Global observations of ocean-bottom subinertial current dissipation. *Journal of Physical Oceanography*, **43 (2)**, 402–417.

Wunsch, C., 1998: The work done by the wind on the oceanic general circulation. *Journal of Physical Oceanography*, **28 (11)**, 2332–2340.

Wunsch, C., and R. Ferrari, 2004: Vertical mixing, energy, and the general circulation of the oceans. *Annu. Rev. Fluid Mech.*, **36**, 281–314.

LIST OF TABLES

TABLE 1. Summary of the simulation parameters for the upslope (u) cases. The slope Burger number $Bu = \frac{\alpha N_\infty}{f}$, friction Reynolds number $Re_* = \frac{u_{*0}^2}{f\nu}$, friction Richardson number $Ri_* = \frac{N_\infty^2}{f^2}$ and Prandtl number $Pr = \frac{\nu}{\kappa}$.

Expt.	α	$\log_{10} N_\infty^2 (\mathrm{s}^{-2})$	$V_\infty (\mathrm{ms}^{-1})$	Bu	Re_*	Ri_*	Pr
A-u	0.005	-7	0.1	0.016	4232	10	5
B-u	0.01	-7	0.1	0.032	4232	10	5
C-u	0.01	-6	0.1	0.1	4232	100	5
D-u	0.01	-5	0.1	0.316	4232	1000	5
E-u	0.02	-6	0.1	0.2	4232	100	5
F-u	0.02	-5	0.1	0.632	4232	1000	5
G-u	0.01	-6	0.05	0.1	1352	100	5
H-u	0.01	-5	0.05	0.316	1352	1000	5

TABLE 2. Summary of the simulation parameters for the downslope (d) cases as studied in Ruan et al. (2019). The parameters are defined in Table 1. Note that the simulations do not only vary the mean flow directions compared with the upslope simulations.

Expt.	α	$\log_{10} N_\infty^2 (\mathrm{s}^{-2})$	$V_\infty (\mathrm{ms}^{-1})$	Bu	Re_*	Ri_*	Pr
A-d	0.005	-7	0.1	0.016	4232	10	5
B-d	0.01	-6.5	0.1	0.056	4232	31.6	5
C-d	0.01	-6	0.1	0.1	4232	100	5
D-d	0.01	-5.5	0.1	0.178	4232	316	5
E-d	0.01	-5	0.1	0.316	4232	1000	5
F-d	0.02	-5	0.1	0.632	4232	1000	5
G-d	0.01	-6	0.05	0.1	1352	100	5
H-d	0.01	-5	0.05	0.316	1352	1000	5

LIST OF FIGURES

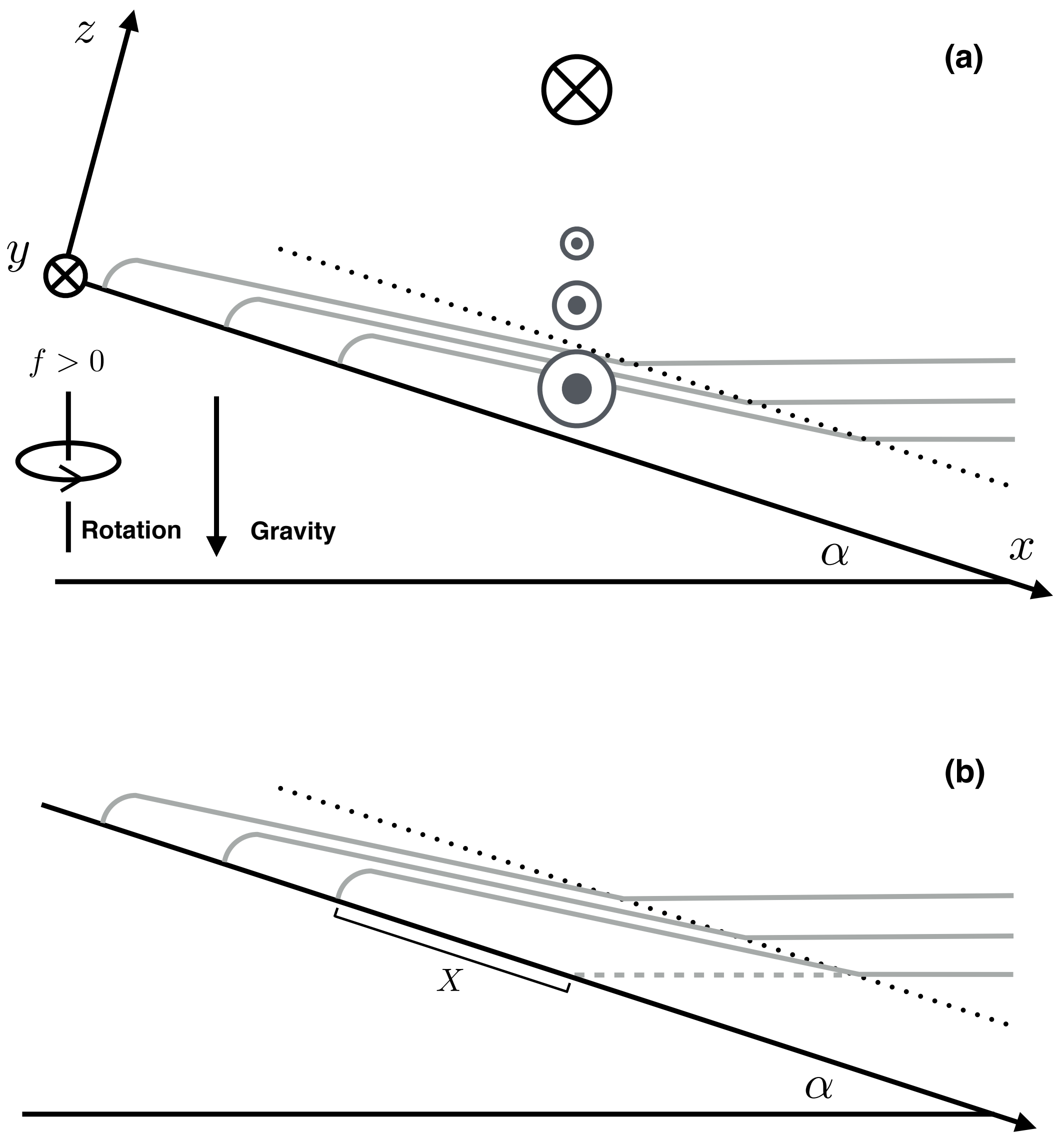

551 FIG. 1. (a) Schematic of the bottom boundary layer over a slope; gray curves indicate density surfaces. The
552 coordinate axes are rotated by a slope angle α. The barotropic mean flow is associated with an upslope Ekman
553 transport. The thermal wind shear generated due to the tilting isopycnals is in the negative *y* direction, opposite
554 to the mean flow. The near-bottom velocity is the sum of the barotropic mean flow and the opposing thermal
555 wind shear. (b) Schematic of the displacement of isopycnals *X* in sloping BBLs. The dashed lines represent the
556 unperturbed isopycnals before they are advected upslope. The dotted lines denote the top of the BML.

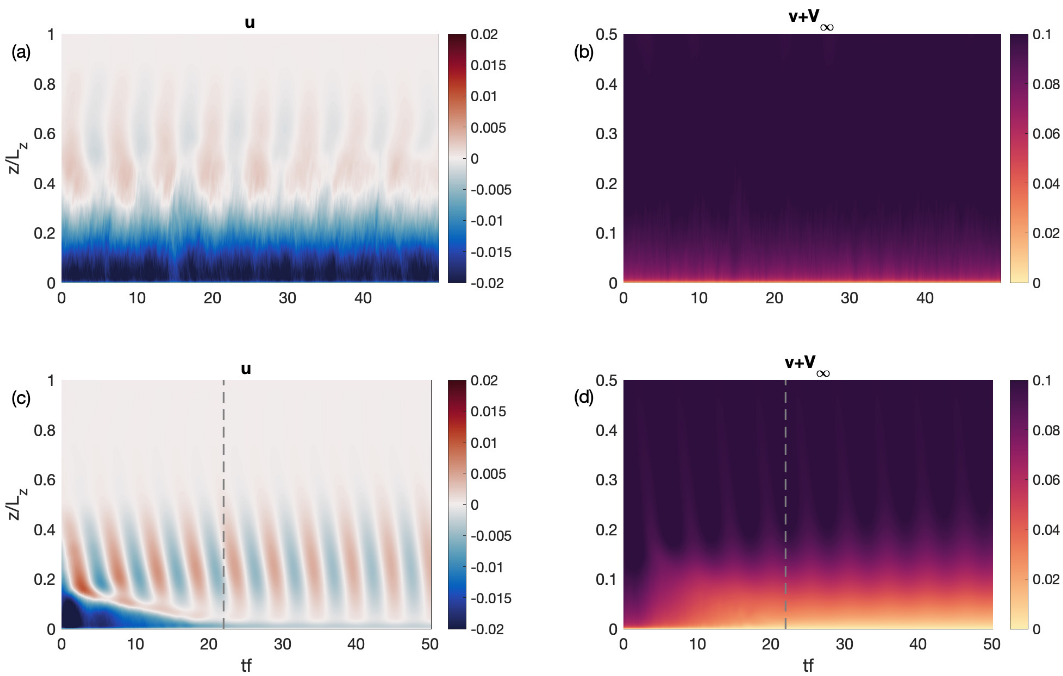

FIG. 2. The evolution of cross- (u) and along-slope ($v+V_\infty$) velocities (m s^{-1}) in simulations A-u and F-u (Table 1). The cross-slope velocities u in simulations A-u and F-u are shown in (a) and (c) respectively. The total along-slope velocities $v+V_\infty$ in simulations A-u and F-u are shown in (b) and (d). The vertical dashed lines in panels (c) and (d) denote the time when the snapshots in Fig. 4 are taken. Time t and depth z are non-dimensionalized by the inertial time scale ($1/f$) and the height of the domain (L_z), respectively.

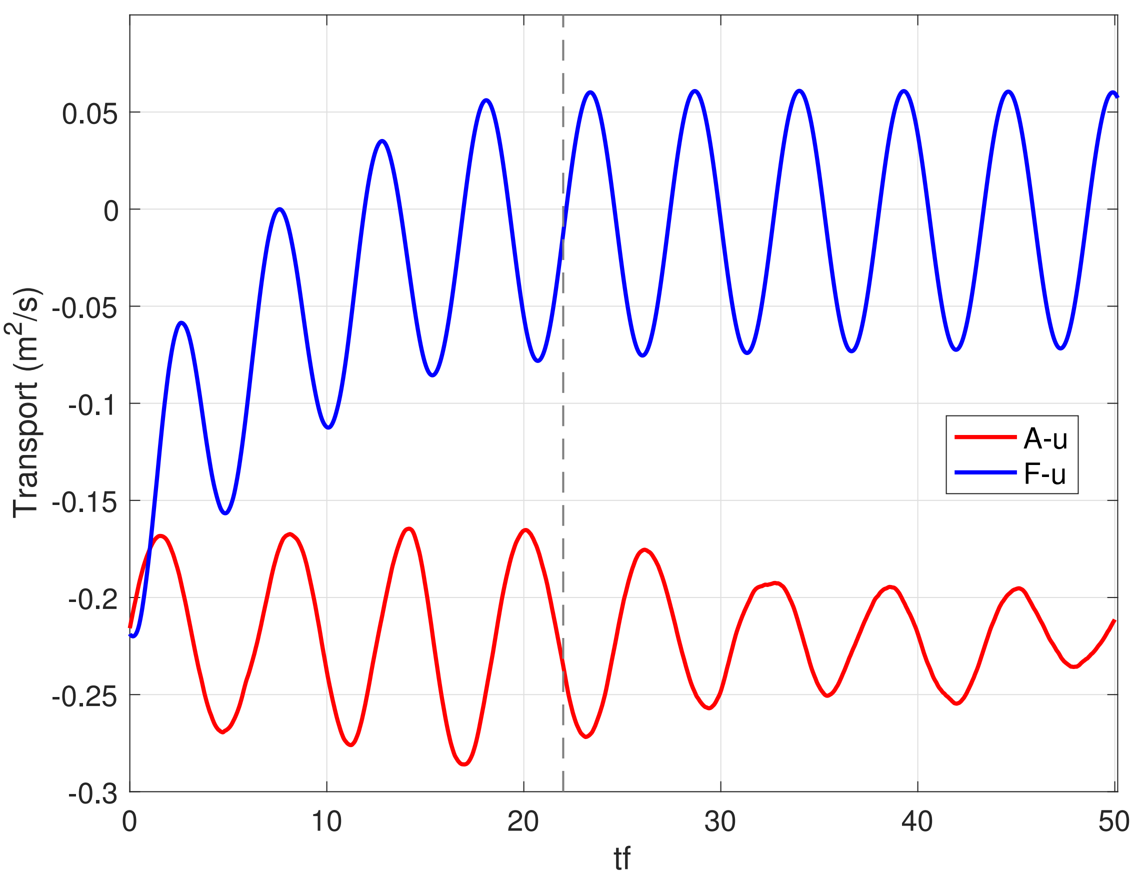

562 FIG. 3. The evolution of cross-slope transport in simulations A-u and F-u (Table 1). The vertical dashed line
563 denotes the time when the snapshots in Fig. 4 are taken.

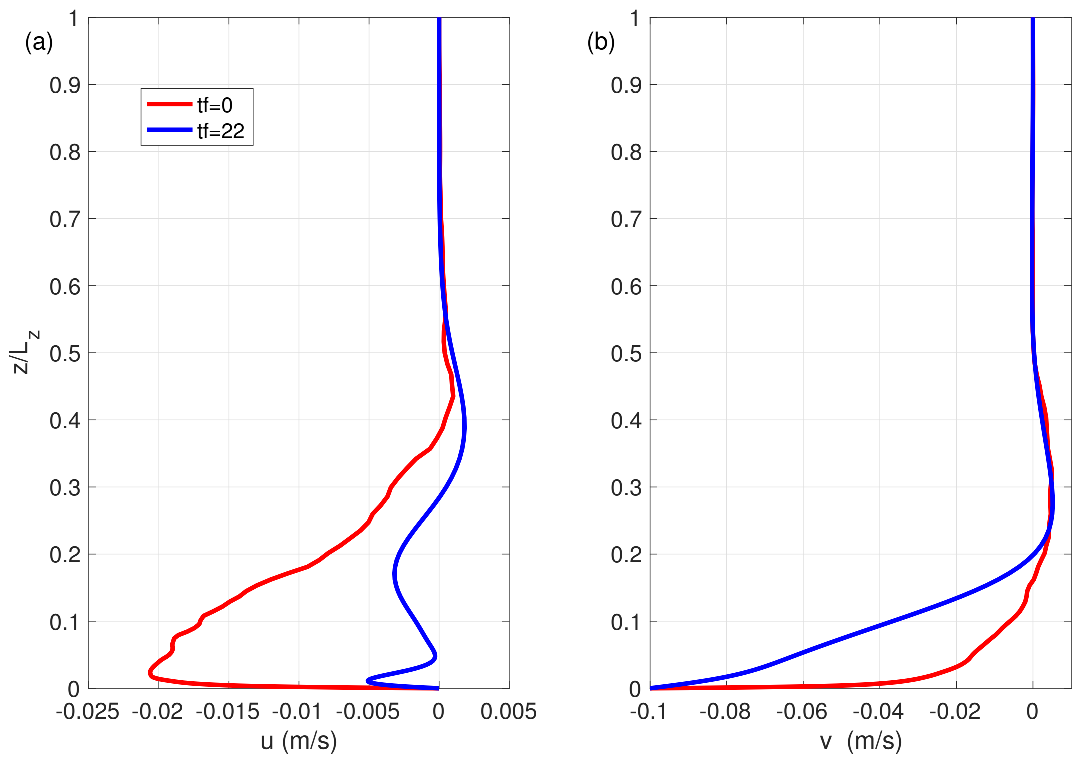

564 FIG. 4. The cross- (a) and along-slope (perturbation) (b) velocities at the beginning and near the end ($tf = 22$) of simulation F-u. The time $tf = 22$ is denoted by the vertical dashed line in Figs. 2 and 3.

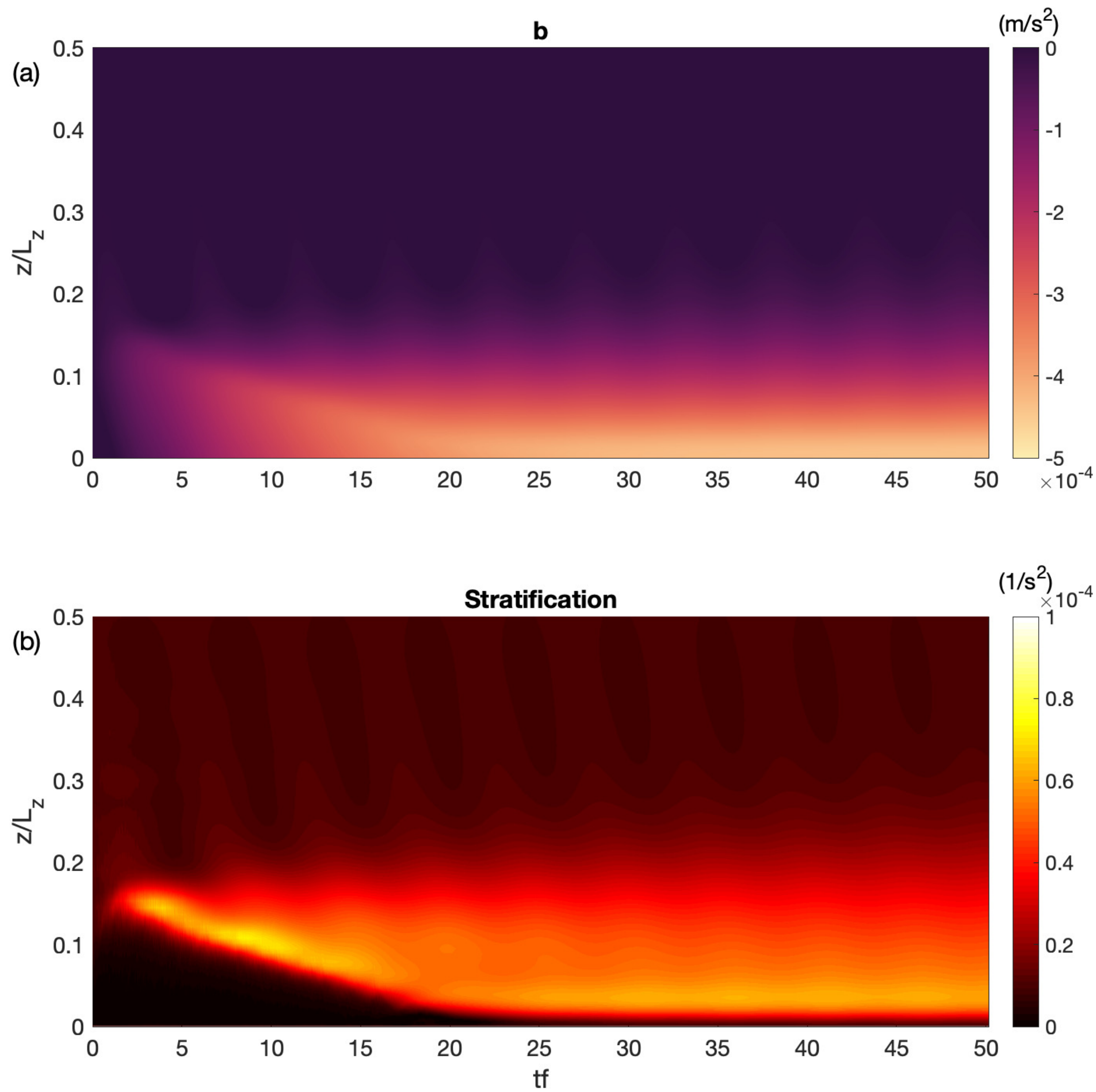

FIG. 5. The evolution of buoyancy (m s^{-2}) (a) and total stratification $b_z + N_\infty^2$ (s^{-2}) (b) in simulation F-u.

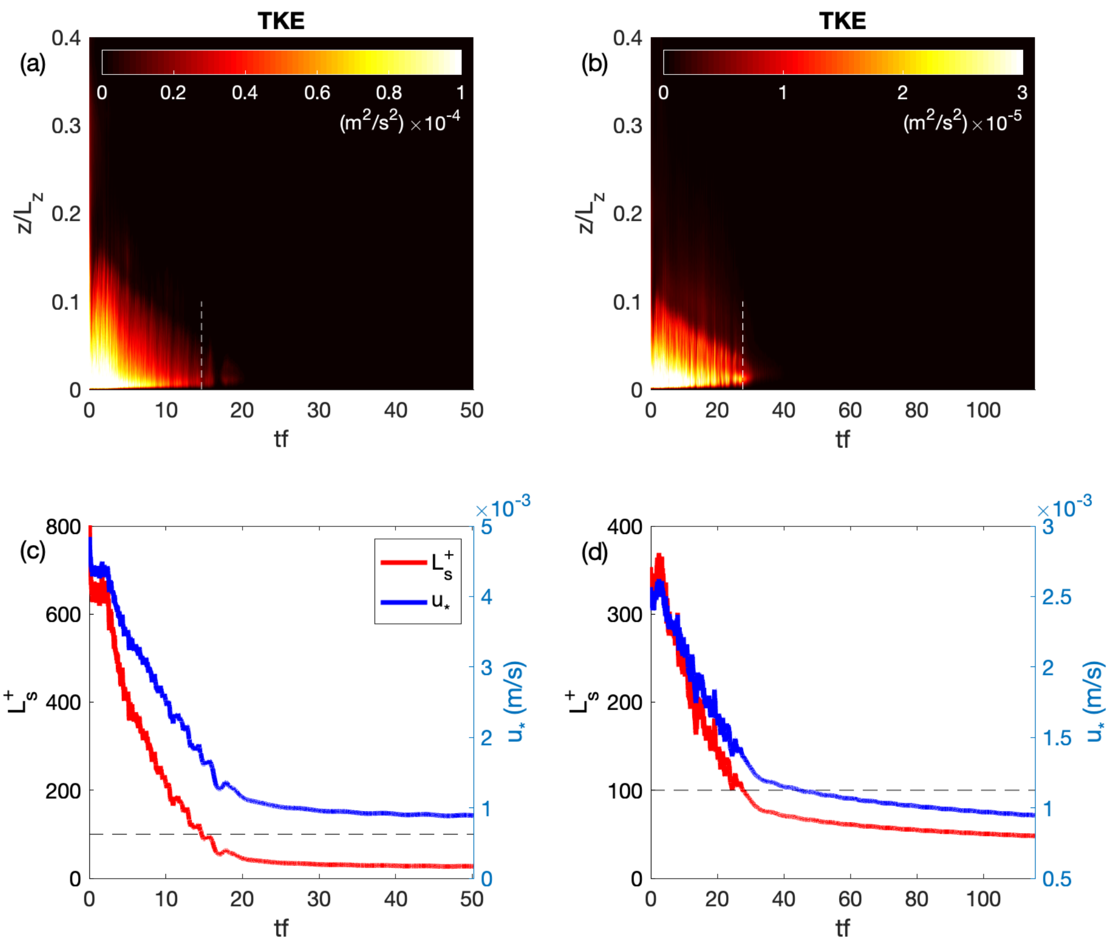

566 FIG. 6. The evolution of TKE (m^2 s^{-2}), L_s^+ (non-dimensional) and u_* (m s^{-1}) in simulations F-u (left panels) and H-u (right panels). The vertical dashed lines in (a) and (b) denote the times when the corresponding L_s^+ fall below 100 and the horizontal dashed lines in (c) and (d) represent $L_s^+ = 100$.

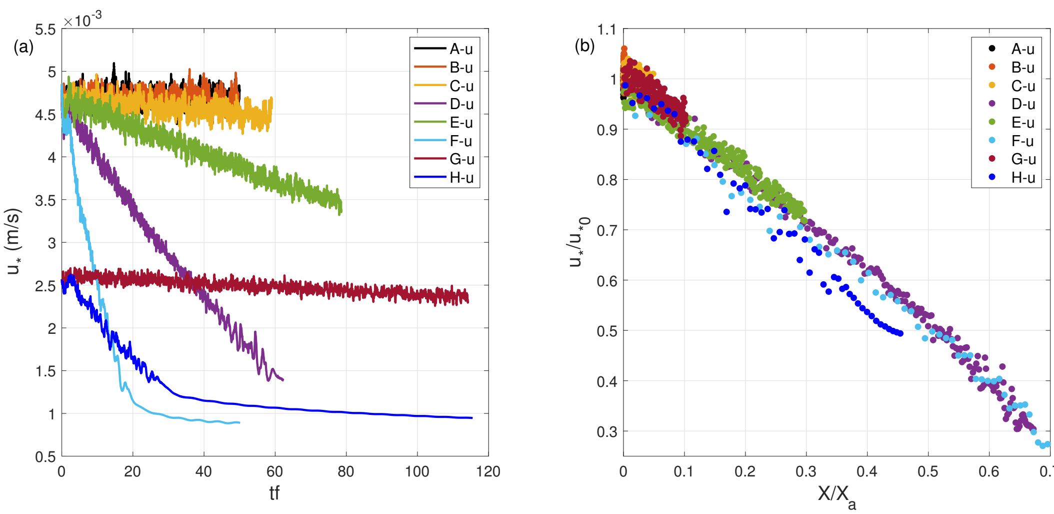

FIG. 7. (a) The evolution of friction velocity u^* as a function of non-dimensional time tf. (b) The evolution of friction velocity u_*, non-dimensionalized by the initial friction velocity u_{*0}, as a function of X/X_a. Different colors represent different simulations in Table 1. The data for when L_s^+ becomes smaller than 100 in simulations F-u and H-u are not included in panel (b).

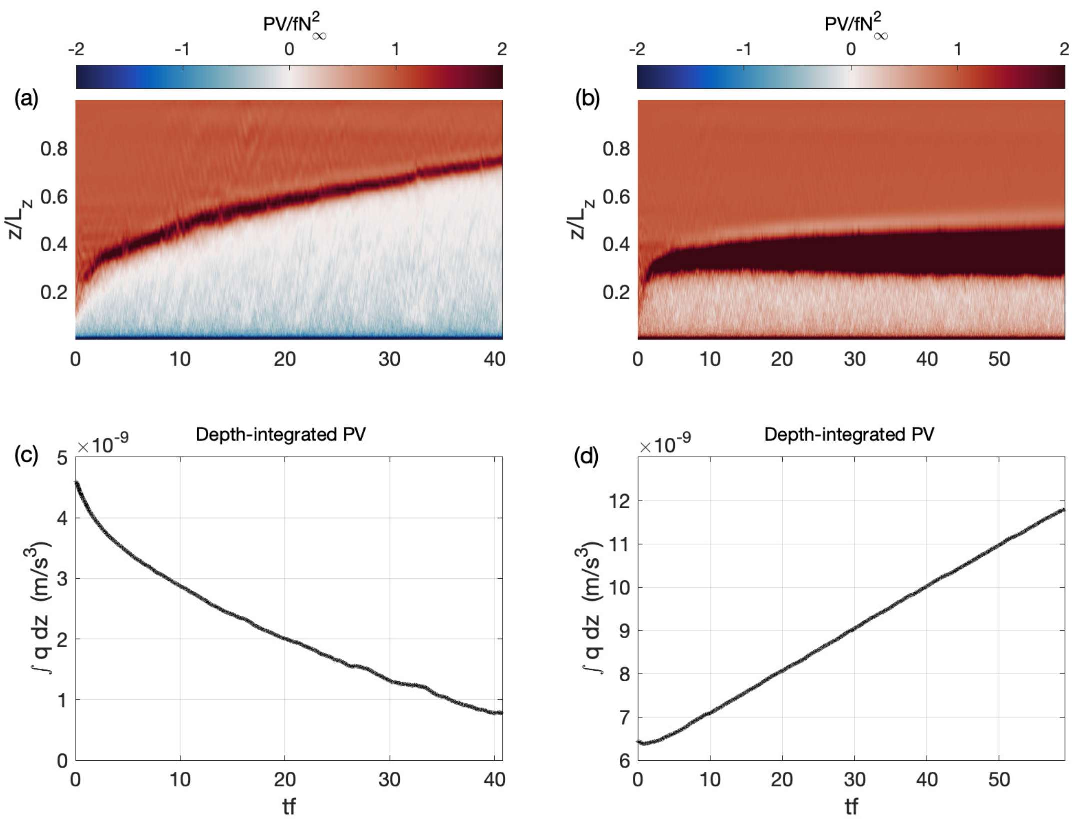

573 FIG. 8. Temporal evolution of PV and depth-integrated PV in simulations C-d in the downwelling regime (left) and C-u in the upwelling regime (right). The PV in (a) and (b) are normalized by fN_∞^2 for the corresponding simulation.

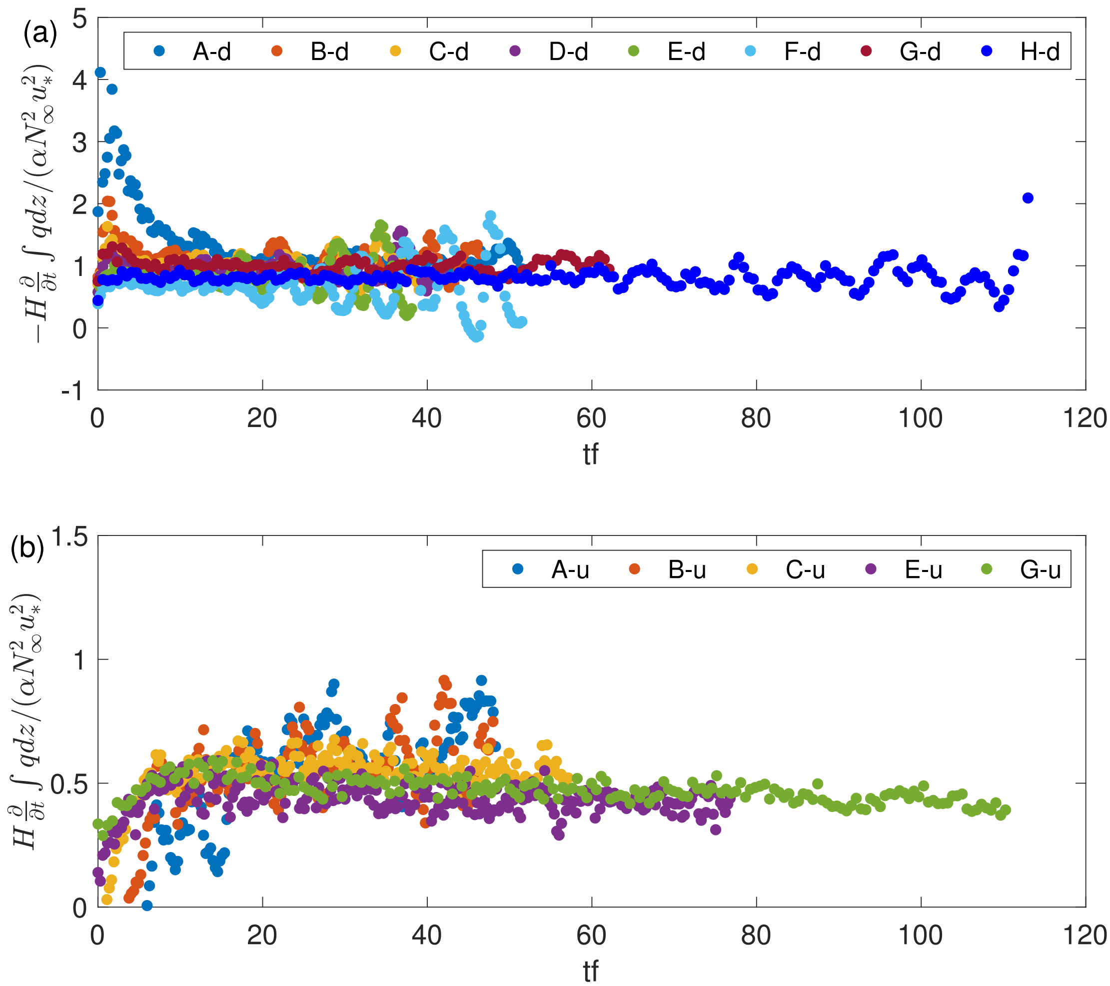

576 FIG. 9. The evolution of the depth-averaged PV destruction rate (a) and the PV production rate (b) normalized by $(\alpha N_\infty^2 u_*^2)/H$ in the downwelling (panel a) and upwelling (panel b) regimes. Different colors represent different simulations in Tables 1 and 2.

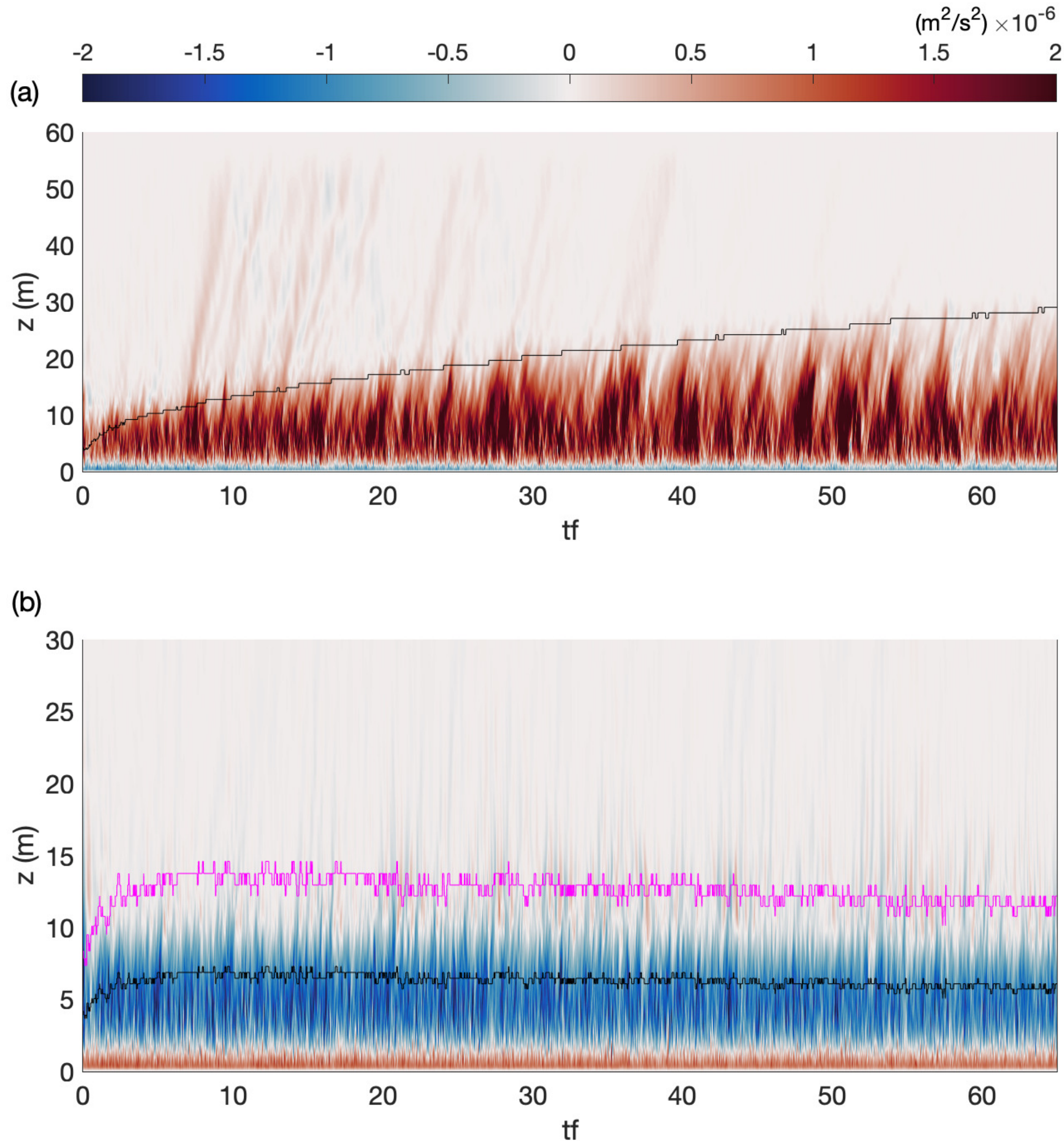

FIG. 10. Temporal evolution of turbulent stresses $< u'w' >$ in simulation G-d in the downwelling (a) and G-u in the upwelling (b) regimes. The black curves denote the BML thickness H based on the diagnosed stratification and the magenta curve in panel (b) represents twice the BML thickness in the upwelling regime.